Proceedings of the ASME 2022
ICE Forward Conference
ICEF2022
October 16-19, 2022, Indianapolis, Indiana

ICEF2022-90501

LAMINAR FLAME SPEED MEASUREMENTS OF PRIMARY REFERENCE FUELS AT EXTREME TEMPERATURES

Adam J. Susa[*]
Mechanical Engineering
Stanford University
Email: asusa@alumni.stanford.edu

Lingzhi Zheng[*]
Mechanical Engineering
Stanford University
Email: liz147@stanford.edu

Zach D. Nygaard
Mechanical Engineering
Stanford University
Email: znygaard@stanford.edu

Alison M. Ferris
Mechanical Engineering
Stanford University
Email: aferris@stanford.edu

Ronald K. Hanson[†]
Mechanical Engineering
Stanford University
Email: rkhanson@stanford.edu

ABSTRACT

Experimentally measured values of the laminar flame speed (S_L) are reported for the primary reference fuels over a range of unburned-gas temperatures (T_u) spanning from room temperature to above 1,000 K, providing the highest-temperature S_L measurements ever reported for gasoline-relevant fuels. Measurements were performed using expanding flames ignited within a shock tube and recorded using side-wall schlieren imaging. The recently introduced area-averaged linear curvature (AA-LC) model is used to extrapolate stretch-free flame speeds from the aspherical flames. High-temperature S_L measurements are compared to values simulated using different kinetic mechanisms and are used to assess three functional forms of empirical S_L–T_u relationships: the ubiquitous power-law model, an exponential relation, and a non-Arrhenius form. This work demonstrates the significantly enhanced capability of the shock-tube flame speed method to provide engine-relevant S_L measurements with the potential to meaningfully improve accuracy and reduce uncertainty of kinetic mechanisms when used to predict global combustion behaviors most relevant to practical engine applications.

INTRODUCTION

The shock-tube flame speed method was developed with the goal of extending the unburned-gas temperature range accessible to laminar flame speed (S_L) measurements [1]. Cutting-edge and next-generation internal combustion engines (ICEs) operate at high temperatures where flame propagation and spontaneous ignition can occur in a coupled manner, jointly governing the performance and operability of the system. Questions and challenges stemming from these extreme conditions have repeatedly appeared in the literature. Twenty years ago, researchers at Ford questioned whether flame propagation occurs in homogeneous-charge compression ignition (HCCI) engines in contrast to conventional wisdom that HCCI engines operate at conditions too lean to support flames even at temperatures exceeding 1,100 K [2]. Researchers at Cummins have similarly reported gaps in the knowledge of high-temperature flames, noting "laminar flame speed data introduces the highest uncertainty in the SI [spark-ignition] combustion modeling process," and "data is usually not available at engine conditions" [3]. Another group from Cummins was the first to report the practical solution of varying the length of the domain used in S_L calculations to address the challenge of predicting S_L at reactive conditions relevant to homogeneous charge spark ignition (HCSI) engines [4], a method since

[*]Co-first authors
[†]Corresponding author

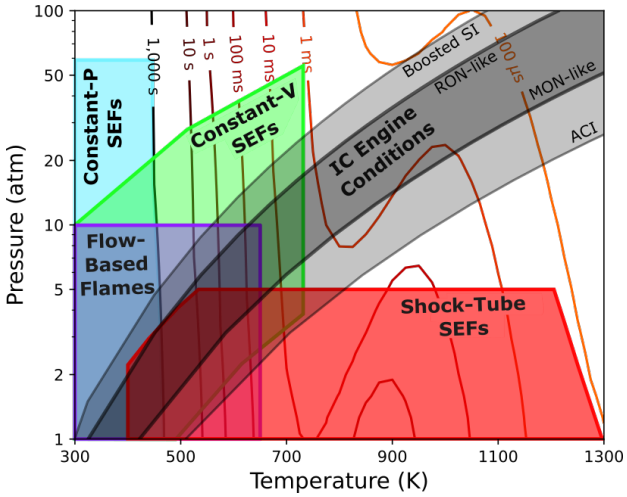

FIGURE 1: TEMPERATURE–PRESSURE REGIMES ACCESSIBLE TO DIFFERENT LAMINAR FLAME SPEED MEASUREMENT APPROACHES

extended through methods of varying complexity [5–11]. The continued relevance of high-temperature flame behavior is illustrated by a recent paper from ANSYS outlining an approach for handling flames at reactive conditions within their computational fluid dynamics (CFD) platform [12].

Experimental S_L measurements have traditionally been limited to low unburned-gas temperatures (T_u) by fuel–oxidizer mixture reactivity. Regimes of T_u–P_u accessible to different experimental techniques are approximated in Fig. 1. Conditions traditionally relevant to IC engines (dark gray) are shown bounded by air-standard isentropic trajectories from the research and motor octane number (RON and MON) intake conditions [13, 14]. An extended engine-relevant regime (light-gray) is shown bounded by isentropes originating from boosted SI and advanced compression ignition (ACI) intake conditions [15].

In the background of Fig. 1, contours of ignition delay time (IDT, τ_{ign}) are shown, as calculated for *n*-heptane at unity equivalence ratio ($\phi = 1$) using a skeletal reaction mechanism [16]. Simulations were performed using Cantera [17] with a zero-dimensional (0-D), constant-pressure reactor model and the onset of ignition defined as a 5 K temperature increase, a definition capable of capturing first-stage ignition when two-stage ignition occurs. Contours of τ_{ign} are intended only to provide an approximate reference for the scaling of reaction timescales with T_u and P_u; for this limited purpose, the reduced accuracy of τ_{ign} values resulted from the use of a skeletal reaction mechanism and simple definition of ignition onset are inconsequential.

Constant-pressure (-P) spherically expanding flames (SEFs, light blue in Fig. 1) have been demonstrated at unburned-gas pressures (P_u) up to 60 atm [18]. However, long equilibration times (order 10 minutes) limit constant-P SEFs to low-T_u conditions at which no spontaneous chemistry can occur; the lack of dynamic compression additionally imposes a fuel-loading limit to the maximum P_u achievable with liquid fuels (not reflected in Fig. 1) [19]. Constant-volume (-V) SEFs (green in Fig. 1) use the isentropic compression of the unburned gas ahead of an expanding flame to dynamically heat and pressurize the mixture. Historically popular with Metghalchi and Keck [20] and Gülder [21] for its ability to access to elevated T_u and P_u before falling out of favor due to high uncertainty, the constant-V SEF method is regaining popularity [22–24]. Modern applications have demonstrated S_L measurements using constant-V SEFs to 720 K [24]; the propensity for autoignition in the unburned gas restricts the method from accessing higher T_u [25]. Flow-based flames (purple in Fig. 1), examples of which include stagnation configurations or diverging channels, provide a third class of experimental techniques. Elevated temperatures approaching those accessible to constant-V SEFs have been demonstrated through the use of inline heating in the flow-delivery device; the displayed T_u limit of 650 K being the highest demonstrated temperature using modern techniques known to the author [26].

The shock-tube flame speed method (red in Fig. 1) utilizes a constant-P expanding flame ignited in the post-reflected-shock environment of a shock tube. Acting as an impulse heater, the use of a shock tube effectively eliminates the heating time of the unburned gas and enables S_L measurements at reactive unburned-gas conditions. The high-temperature limit in Fig. 1 is based on an estimated reactivity limit of ($Da_m \equiv \tau_m/\tau_{ign} < 0.1$), where Da_m is the measurement Damköhler number and $\tau_m \approx r_{f,m}/S_b^0$ is the time required for an expanding flame to reach the radius $r_{f,m}$ needed to perform a measurement. Here, $r_{f,m} = 1$ cm is used and S_b^0, the unstretched, burned-gas flame speed, is estimated using a power-law correlation for *n*-heptane–air flame speeds with parameters from a recent review [27]. The 5-atm pressure limit is a conservative limit for the imaging shock tube in which the present measurements were performed. The present facility has since been demonstrated to be compatible with autoignition-induced dynamic pressures of 10 atm [28] and emission imaging has previously been demonstrated to 20 atm or more in high-pressure shock-tube facilities [29, 30], such that potential pathways exist to access much higher pressures in future studies.

Early applications of the shock-tube flame speed method were limited in the temperatures they accessed [1] or incurred elevated uncertainty in the interpretation of measurements [31–33] as a result of flame wrinkling and distortion [34, 35]. However, subsequent studies have provided significant new insights into the post-reflected-shock environment [36] and conditions under which suitably stable and undistorted flames can be produced [35, 37]. Through these learnings and the availability of refined diagnostics [38, 39], S_L measurements have since been demonstrated in the shock tube at temperatures up to 1,200 K for propane [40–42], the highest-T_u measurements ever reported for any fuel. In this work, these same refined methods

are applied to the study of primary reference fuels at temperatures spanning from room temperature up to 1,000+ K, revisiting and expanding upon T_u conditions investigated in earlier studies [10, 11, 31–33, 43, 44] in order to clarify prior observations and provide reliable S_L measurements for these gasoline-relevant fuels at engine-relevant temperatures.

EXPERIMENTAL METHODS

In this section, the instrumentation and analysis employed in the shock-tube flame speed method, as implemented in the present study, are described. A comprehensive discussion of the efforts through which the shock-tube flame speed method, first reported by Ferris *et al.* [1], has been characterized and refined is provided by Susa [45]. The specific methodology applied in this work was first reported and validated in its application to the study of propane flame speeds [41, 42].

Overview of Shock Tube Techniques

In this work, a shock-tube serves as an impulse heater to nearly instantaneously heat the fuel–oxidizer mixture to the unburned-gas conditions at which an S_L measurement is performed. The progression of a shock-tube experiment is represented in Fig. 2. Initially (Fig. 2a), a polycarbonate diaphragm separates the driven section (right, region-1), filled to low-pressure with the premixed fuel–oxidizer test-gas mixture, from the driver section (left, region-4), filled with inert driver gas to higher pressure. The experiment begins when the pressure difference ($P_4 - P_1$) presses the diaphragm into a cutter, causing it to rupture. As shown in Fig. 2b, the rupture of the diaphragm results in a shock wave propagating into the test gas that heats, pressurizes, and accelerates it to region-2 conditions. Upon reaching the end wall, the shock wave reflects (Fig. 2c), substantially stagnating the test gas [36] while further heating and pressurizing it to the region-5 conditions at which the S_L measurement is performed ($T_5 = T_u$, $P_5 = P_u$).

Premixed fuel–oxidizer test-gas mixtures are prepared manometrically from research-grade liquid fuels and a certified-standard mixture (supplied by Praxair) of 21% O_2, 79% Ar; the use of Ar dilution is a common provision for shock-tube experiments and was specifically informed for use in flame speed experiments by the analysis of [35]. The liquid fuel was degassed at cryogenic temperatures prior to being vaporized at room temperature into an initially evacuated mixing tank and subsequently diluted with the oxidizer. Stoichiometric mixtures were prepared based on manometric component measurements, providing a mixture Lewis number (Le) above unity as required to stabilize expanding flames against thermo-diffusive instabilities. Fuel mole fractions, which vary as a result of adsorption to the mixing tank and shock tube walls, is quantified *in-situ* for each experiment through a region-5 fuel measurements using a 3.41-μm

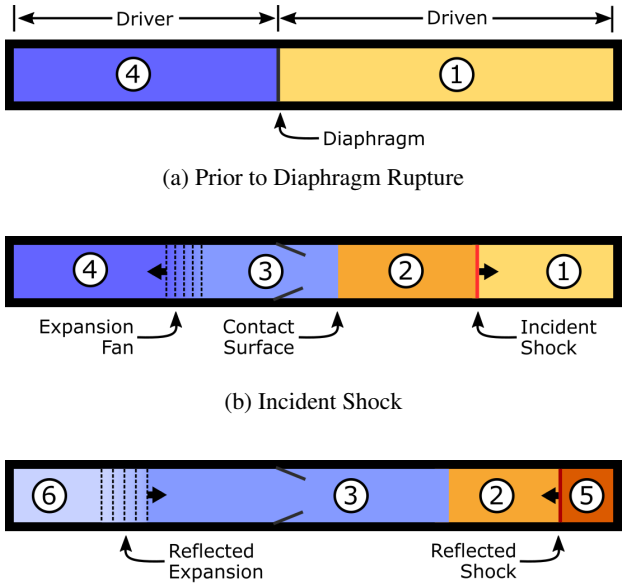

(a) Prior to Diaphragm Rupture

(b) Incident Shock

(c) Reflected Shock

FIGURE 2: ANNOTATED THERMODYNAMIC REGIONS OF A SHOCK-TUBE EXPERIMENT

laser absorption diagnostic [46]. Equivalence ratios (ϕ) based on measured mole fractions are typically somewhat lean ($\phi < 1$), leading to somewhat higher Le. Region-5 conditions are calculated using the in-house FROSH code that solves the normal shock equations using an incident shock speed measured with a time-of-arrival technique using PCB pressure transducers arrayed along the driven section and extrapolated to the end wall to account for shock attenuation [47].

Various mixtures of He and N_2 driver gases were used to generate the different shock strengths required to conduct measurements over a wide range of T_5. Two diaphragm thicknesses were required to provide coverage over the entire temperature range of interest. A driver insert [48], designed in simulation using the open-source StanShock code [49], was used together with the thicker diaphragm (0.010 inch) to counteract the pressure rise (dP/dt) in high-T_5 experiments. A single insert was found to perform satisfactorily well over all T_5 conditions when P_1 and the shock strength were varied to maintain a consistent $P_5 \approx 1$ atm. With the thinner diaphragm (0.005 inch) used for low-T_5 experiments, a slight, negative dP/dt was observed in region-5 and thus no insert was used. To perform the room-temperature S_L measurements, the gate valve (Fig. 3) was closed to isolate the test section; the test section was filled to P_u with the fuel–oxidizer mixture and a flame was ignited under static conditions.

Facility and Instrumentation

The side-wall imaging flame test section (SWIFT, shown in Fig. 3) was recently introduced [37, 38], providing side-wall optical access for schlieren imaging within a round shock tube. The defining side-wall windows are designed as zero-power, aberration-corrected, cemented-doublet cylindrical lenses. The inner radius of curvature matches the 11.53-cm diameter of the shock tube, while the curvatures of the outer surface and interface separating the fused-silica inner element from the BK-7 outer element were selected to provide low aberration at the 550-nm design wavelength. The side-wall windows provide a maximum 18- by 5-cm schlieren-compatible side-wall field of view (FOV) into the shock tube. 20-cm long by 2-cm wide slot windows provide access for the ignition laser over a continuous range of axial positions. The axial position of the spark within the tube was adjusted for different ranges of T_u in order to find locations producing stable, minimally distorted flames [37].

Flames are non-intrusively ignited within the shock tube through laser-induced plasma ignition (LIPI) [50–52]. Details of the system used in this work have been previously reported [37, 38]; the system is shown schematically in Fig. 3a and described here in brief. A nanosecond-pulsed, Q-switched, frequency-doubled (532-nm) Nd:YAG laser (New Wave Research, Solo 120 PIV) serves as the laser source, which is triggered to ignite the flame within 0.5 ms of the reflected shock passing a PCB pressure transducer near the measurement location, a time short relative to τ_{ign} at all T_u studied. A variable polarizing attenuator (Thorlabs model VA5-532) is used to control the energy of the laser pulse that is focused by a 15-cm best-form bispherical lens to a waist (estimated 10-µm diameter) at the center of the tube, where laser-induced breakdown (LIB) occurs, igniting an expanding flame. Energy meters on the pitch and catch sides of the tube provide a differential estimate of the energy lost from the laser pulse to the spark. Typical spark energies in this work were estimated to fall in the range 1–2 mJ, of which only a fraction is expected to be available as thermal energy to support ignition [51].

The propagation of expanding flames ignited in the SWIFT is recorded using a large-FOV, modified Z-fold schlieren imaging system (Fig. 3b); details of the process by which the components of the schlieren system were selected are provided by Zheng *et al.* [39]. Off-axis parabolic (OAP) mirrors with a 4-inch-diameter, 32.7-cm effective focal length, and 30° off-axis angle (Edmund Optics 35-584) collimate and refocus light from a high-power, 528-nm light-emitting diode (LED). The LED is masked by a 500-µm pinhole to reduce the effective size of the source and improve image sharpness. The schlieren optical path is folded on the catch side by a flat mirror for compactness. A 1-mm pinhole at the focal point is used as a schlieren stop to provide isotropic sensitivity to the density gradients of all orientations [53], which enables the consistent detection of the complete flame-front boundary [41, 42].

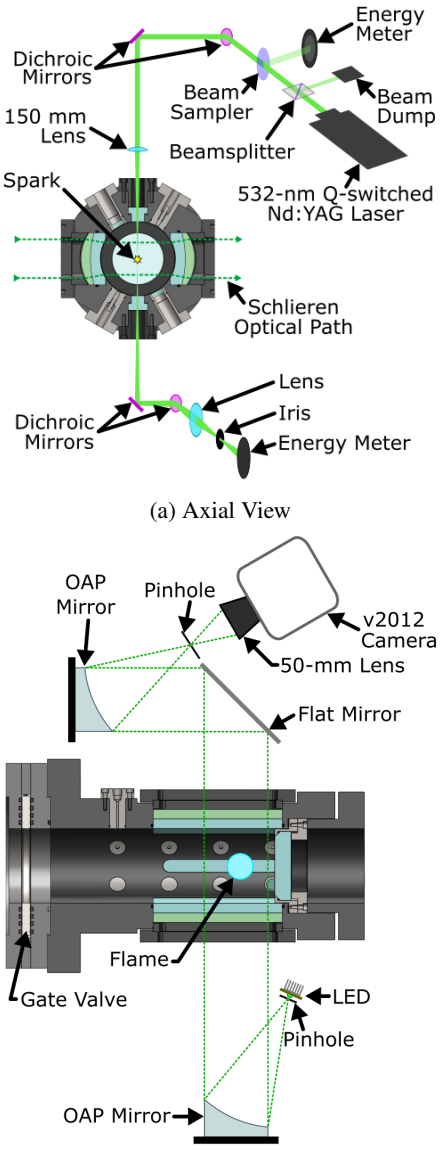

FIGURE 3: CROSS-SECTIONAL VIEWS OF SWIFT AND EXPERIMENTAL INSTRUMENTATION

Schlieren images are recorded through a 50-mm-focal-length Nikkor lens by a Phantom v2012 high-speed camera. The camera records frames at 100,000 fps using a cropped, 512- by 336-pixel sensor region. In the present configuration, side-wall schlieren images are recorded with a roughly 9- by 5-cm FOV and 56 pixel/cm spatial resolution. The steps involved in processing and extracting flame speeds from the recorded schlieren images is the topic of the subsection that follows.

Image and Data Processing

The laminar flame speed, S_L, is defined as the propagation speed (S) of an uncurved and unstretched (superscript 0) flame relative to the unburned (subscript u) reactants (*i.e.,* $S_L = S_u^0$). Meanwhile, the speed of outwardly propagating flames is observed relative to burned gas (S_b) and perturbed by the presence of stretch and curvature effects. Therefore, the goal of data processing is to extract a measured value S_u^0 using values determinable from sequences of flame images. Using a previously described and validated method, of which key details are repeated in this section, flame contours are optimized to processed schlieren images and subsequently utilized in an area-averaged formulation of the linear-curvature model (AA-LC model) to extrapolate the zero-curvature flame speed [41,42].

Schlieren images recorded in the native "cine" format are read into Python and processed using the open source pycine [54] and Scikit-Image [55] packages, respectively. Raw images (Fig. 4a) are spatially and temporally smoothed by a 3-D Gaussian filter to reduce noise prior to pixel-wise background normalization (Fig. 4b) using a pre-shock background image. Temporal differencing is then applied to the images, wherein each frame j has subtracted from it and earlier frame, $j - \delta j$ (with $\delta j \sim 5$ typical); the differencing of temporally correlated images has the beneficial effect of removing slow-varying image artifacts and making the background intensity nominally zero. Positive values of the differenced intensities are truncated to zero, leaving only the negative schlieren signal unique to frame j (Fig. 4c). The differenced image is then overlaid with a diffusely filtered copy (Fig. 4d) of itself to aid the active contouring routine employed in the step that follows.

Once processed, a distortion-correction transformation is applied to the flame images. Following the alignment of the schlieren imaging diagnostic, an image is recorded of a dot-grid calibration target positioned vertically within the shock tube. The target is comprised of black dots printed on transparent film and mounted between sheets of clear polycarbonate, such that the dots block the light from the schlieren source, leaving the pattern of dark dots in the bright-field image (Fig. 5a). Dot locations (spaced 5 mm center to center) are detected by referencing the target image to a background image and performing morphological feature detection in the resulting image. A distortion correction transformation is then calibrated as a mapping of detected dot coordinates to the coordinates of an undistorted grid of constant spacing [39,56,57]. The application of the calibrated transformation (Fig. 5b) then has the effect of both correcting distortion in the images and calibrating the physical scaling of the images. It is notable that Fig. 5 displays considerably greater distortion than seen in Zheng *et al.* due to the presence of the side-wall windows in this study, which result in recorded images being vertically stretched, but not in the original characterization of the schlieren system [39], where distortion was attributable solely to the use of OAP mirrors.

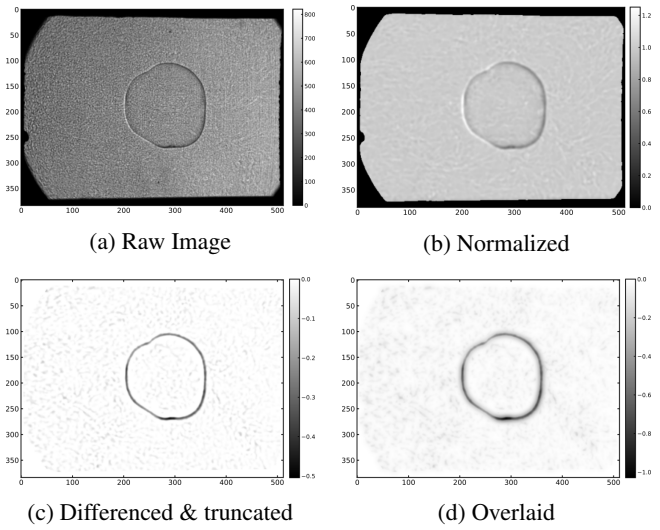

(a) Raw Image (b) Normalized

(c) Differenced & truncated (d) Overlaid

FIGURE 4: IMAGE APPEARANCE AT SELECT STAGES OF PROCESSING

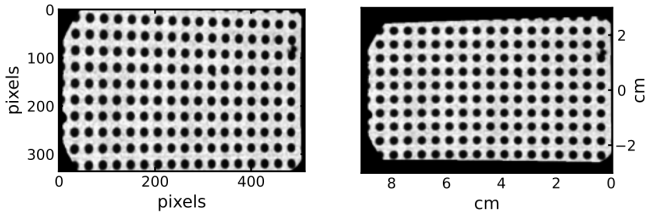

(a) As recorded (b) Corrected

FIGURE 5: DOT-GRID CALIBRATION TARGET IMAGES

Flame-front positions are precisely extracted from processed images using active contouring [58] applied to each frame of the video sequence (Fig. 6a). Defining the horizontal direction, z, as the assumed axis of rotational symmetry,

$$r_f(z) = \frac{D_y(z)}{2}, \tag{1}$$

where $D_y(z)$ is the total vertical extent of the optimal contour at position z and $r_f(z)$ is the corresponding rotationally symmetric value (Fig. 6b). From the approximate, rotationally symmetric flame profile, integrated properties are evaluated:

$$V_b = \pi \int_0^{z_f} r_f^2 \mathrm{d}z, \tag{2}$$

$$A_f = 2\pi \int_0^{z_f} r_f \sqrt{1 + r_f'^2}\,\mathrm{d}z, \tag{3}$$

$$\bar{\kappa} = \frac{1}{A_f} \int_0^{z_f} \kappa(z) r_f \sqrt{1 + r_f'^2}\,\mathrm{d}z, \tag{4}$$

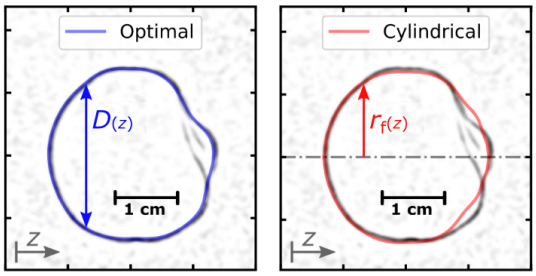

FIGURE 6: OPTIMAL FLAME-FRONT CONTOUR AND CYLINDRICALLY SYMMETRIC APPROXIMATION

where V_b is the burned-gas volume, A_f is the total flame-front area, and $\bar{\kappa}$ is the area-averaged flame-front curvature. The local, total curvature, κ, in Eqn. 4 is taken as

$$\kappa(z) = \frac{-r_f''}{\left(1+r_f'^2\right)^{3/2}} + \frac{1}{r_f\left(1+r_f'^2\right)^{1/2}}, \tag{5}$$

with r_f' and r_f'' being the first and second derivatives of r_f with respect to z, respectively.

The linear-curvature (LC) model,

$$S_b = \begin{cases} S_b^0\left(1-L_b\kappa\right), & \text{general form,} \quad (6a) \\ S_b^0\left(1-L_b\dfrac{2}{R_f}\right), & \text{spherical limit,} \quad (6b) \end{cases}$$

has been shown to provide favorable results extrapolating the stretch-free values S_b^0 from spherically expanding flames of positive L_b (Le > 1) [59,60]. Here, $S_b = S_b(\kappa)$ is the stretched flame speed and L_b is the Markstein length, which can be positive or negative and describes the response of the flame to curvature. In the limit of a spherical flame of radius R_f, the curvature is constant at all points on the surface ($\kappa = 2/R_f$) and Eqn. 6b can be utilized. In order to facilitate its correct application in obtaining measurements from asymmetric flames, the general form (Eqn. 6a) must instead be retained, which is applied in the present work through the AA-LC formulation,

$$\bar{S}_b = S_b^0\left(1-L_b\bar{\kappa}\right), \tag{7}$$

as derived in [41,42] based on $\bar{\kappa}$ from Eqn. 4 and with the average burning rate, $\bar{S}_b$, defined as:

$$\bar{S}_b \equiv \frac{\dot{V}_b}{A_f}. \tag{8}$$

In applying the AA-LC model fits, extracted property data (V_b, A_f, $\bar{\kappa}$) are temporally smoothed, and V_b differentiated, using Savitzky-Golay type filters [61] as implemented in Scipy [62]. Linear fits are then performed to the $\bar{S}_b$–$\bar{\kappa}$ data, providing the Markstein length (L_b) as the slope and S_b^0 as the Y-intercept; uncertainties are taken as the 95% confidence interval of the relevant parameters. Data included in the fit are typically constrained to a range 1.14 cm^{-1} $\leq \bar{\kappa} \leq$ 4 cm^{-1}, corresponding to a radius range of 0.5–1.75 cm. The lower radius limit is selected to avoid spark-energy effects and the upper limit is selected to be 30% of the shock-tube radius based on the cylindrical-confinement criteria of Burke *et al.* [63]. The fit range is adjusted when necessary to avoid the onset of significant distortion or instability of the flame. Finally, S_u^0 is determined from S_b^0 through continuity of the mass burning flux, $\dot{m}_f$ [64],

$$\dot{m}_f = S_b^0\rho_b = S_u^0\rho_u, \tag{9}$$

$$S_u^0 = S_b^0\left(\frac{\rho_b}{\rho_u}\right) = S_L, \tag{10}$$

where ρ_u is evaluated at the unburned-gas conditions and ρ_b is evaluated at the constant-pressure thermochemical equilibrium.

RESULTS AND DISCUSSION

Shock-tube flame speed measurements experiments were performed using *n*-heptane and *iso*-octane fuels over a wide range of temperature conditions, for which results are presented in this section. AA-LC extrapolations of the $\bar{S}_b$–$\bar{\kappa}$ data are shown in Fig. 7 for a subset of the experiments and for all experiments in the Appendix (Fig. 9 and 10). The waviness in the data occurs with a period longer than that of the smoothing filter. While a broader filter could have further reduced the noise, the linear fit is ultimately insensitive to the periodic variations so more aggressive filtering was not performed, instead favoring a more conservative approach whereby the remaining oscillations are allowed to contribute to the uncertainty of the fit. Shaded regions about the best-fit lines represent the 95% confidence interval of the fits, represented by the vertical error bars of the result plots (Fig. 8).

Measurements of *n*-heptane (Fig. 8a) were performed in 1 static experiment and 21 shock experiments conducted over the range 505 K $\leq T_5 \leq$ 1,100 K. Across *n*-heptane experiments, P_u was maintained in the range 0.93 atm $\leq P_5 \leq$ 1.06 atm (mean = 0.99 atm; std. dev. = 0.03 atm) and equivalence ratios, based on *in situ* fuel measurements, fell in the range $0.85 \leq \phi \leq 1.05$ (mean = 0.90; std. dev. = 0.05). Measurements of *iso*-octane (Fig. 8b) were performed in 1 static experiment and 24 shock experiments conducted over the range 577 K $\leq T_5 \leq$ 1,049 K. Across *iso*-octane experiments, P_u was maintained in the range 0.94 atm $\leq P_5 \leq$ 1.06 atm (mean = 1.00 atm; std. dev. = 0.03 atm) and equivalence ratios fell in the range $0.90 \leq \phi \leq 1.08$

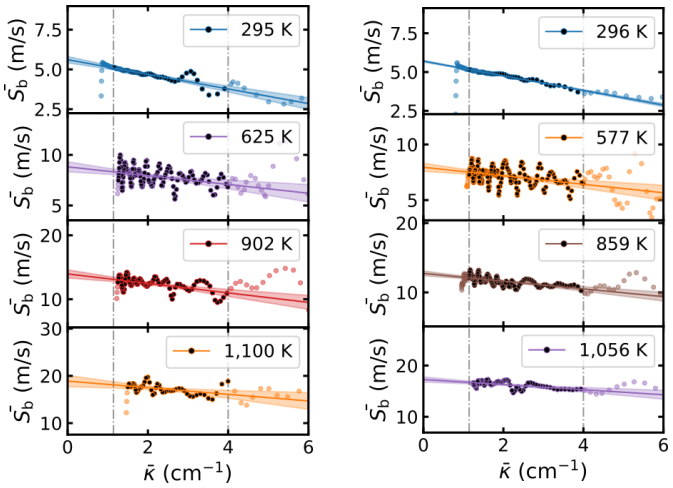

(a) *n*-heptane (b) *iso*-octane

FIGURE 7: AA-LC EXTRAPOLATIONS OF $\bar{S}_b$–$\bar{\kappa}$ DATA FOR SELECT EXPERIMENTS

(mean = 0.95; std. dev. = 0.04). Detailed conditions for each experiment, along with estimated uncertainties of the experimental parameters and corresponding results, are tabulated in the Appendix (Tables 2 and 3).

The measured S_L values in the top axes of Fig. 8a and 8b are shown overlaid on empirical fits performed to S_L measurements of $T_u < 850$ K (filled markers) and functionally constrained to coincide with the measured, room-temperature S_L value. Three functional forms of empirical fits are considered:

$$S_{L,\text{power law}} = S_{L,0}\left(\frac{T_u}{T_0}\right)^{\alpha}, \tag{11}$$

$$S_{L,\text{exponential}} = S_{L,0}\ \exp\left(\frac{T_u - T_0}{T_{\text{exp}}}\right), \tag{12}$$

$$S_{L,\text{non-Arrhenius}} = S_{L,0}\left(\frac{T_u}{T_0}\right)^{\alpha} \exp\left(\frac{T_u - T_0}{T_{\text{exp}}}\right). \tag{13}$$

The fitting parameters — reference speed $S_{L,0}$, temperature exponent α, and characteristic temperature T_{exp} — evaluated with a reference temperature $T_0 = 300$ K, are tabulated for both fuels and all three functional forms in Table 1. Residuals, defined as the percentage difference of measured values S_L as compared to the empirical fits, are shown in the bottom axes of Fig. 8a and 8b.

Among the three forms considered, only the non-Arrhenius form is able to systematically capture the temperature dependence of the data over the range 300–850 K. The ubiquitous power-law and simple exponential fits both show systematic variations in the residuals, trending between about ±10% (light gray band). These systematic trends indicate that the functions fail

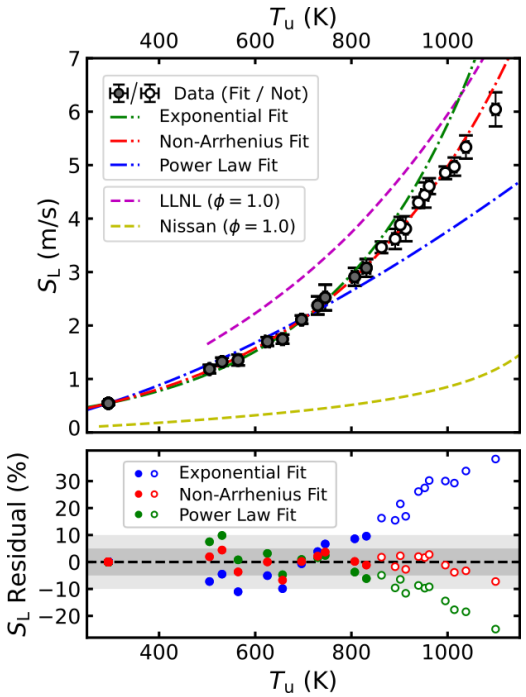

(a) *n*-heptane

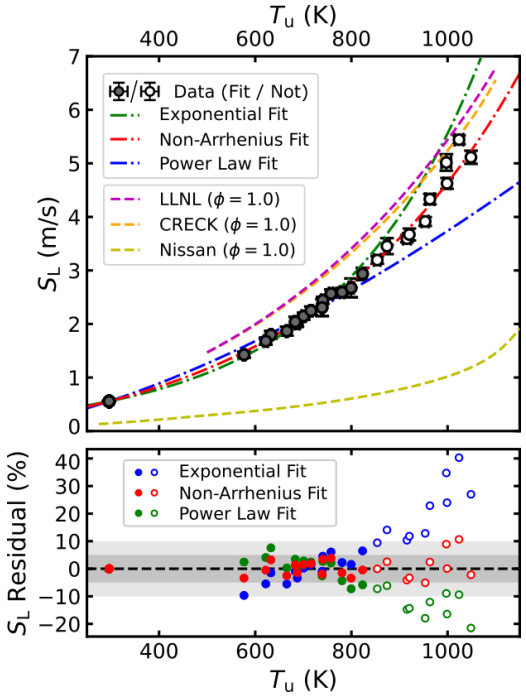

(b) *iso*-octane

FIGURE 8: MEASURED LAMINAR FLAME SPEEDS, EMPIRICAL FITS, SIMULATION RESULTS, AND RESIDUALS

TABLE 1: EMPIRICAL FITTING PARAMETERS

Empirical Form	$S_{L,0}$ (cm/s)	α (–)	T_{exp} (K)
n-heptane			
Power Law	56.1	1.58	–
Exponential	55.6	–	299
Non-Arrhenius	55.8	0.56	461
iso-octane			
Power Law	56.7	1.57	–
Exponential	56.3	–	306
Non-Arrhenius	56.5	0.72	567

to accurately capture the underlying temperature dependence of the measured values S_L. Conversely, the non-Arrhenius form, which adds a third fitting parameter by combining the power-law and exponential forms, systematically captures the temperature trends, with residuals randomly distributed about zero and typically below 5% in magnitude (darker gray band).

Extrapolating to T_u above 850 K and comparing to S_L data not considered when performing the fits, the non-Arrhenius model continues to perform favorably, maintaining residuals within 10% at T_u as high as 1,100 K. On the other hand, the performance of the power-law and empirical models continues to degrade, with the power-law model under predicting the data by as much as 40% at the highest temperatures. The poor performance of the power-law model comes despite the fact that the optimal values α found in the power-law fits of 1.58 and 1.57 for *n*-heptane and *iso*-octane, respectively, are well within the range of values typically reported for mixtures of the same fuels with air [27]. In this way, these S_L measurements illustrate the significant risk for error introduced when empirical models are applied outside the ranges over which they are validated, a common result of the historical lack of high-T_u measurements.

Figures 8a and 8b also include representative simulated flame speeds obtained from 1-D laminar flame speed simulations performed in the PREMIX module of ANSYS Chemkin 18.2. Values of S_L were calculated for both fuels with detailed mechanisms from LLNL: *n*-heptane v3.1 in Fig. 8a and *iso*-octane v3 in Fig. 8b [65, 66]. Reduced mechanisms were additionally evaluated from the CRECK group for *iso*-octane [67–69] and for both fuels using a mechanism from Tsurushima of Nissan, to which Ar was added for use in the present work [70]. An effort was made to include comparisons to simulations using the new detailed C3MechV3.3 mechanism [71], but solutions could not be found by Chemkin for this extremely large mechanism. Simulated values shown in Fig. 8a and 8b were obtained at $P_u = 1$ atm and $\phi = 1$ using short simulation domains (≈ 1 cm) to preclude spontaneous chemistry affects on the calculated values [5].

The simulation comparisons provide a first opportunity to evaluate the capabilities of kinetic mechanisms for predicting PRF $S_L$at very high-T_u conditions. The detailed LLNL mechanisms are found to over predict the measured values S_L for both fuels. While discrepancies of about 10% may be attributed to the variable, typically lean ϕ seen in experiments as compared to the stoichiometric ϕ used in simulation, observed discrepancies are larger, suggesting a potential opportunity for refinement to the mechanisms. The reduced CRECK mechanism is found to produce close agreement with that from LLNL for *iso*-octane, again over predicting the measured S_L. The most remarkable disagreement is seen in the Nissan PRF mechanism developed for HCCI engine conditions, which under predicts the measured S_L values by a factor of 3–4 over the studied temperature range. Even though this mechanism was optimized for higher-pressure conditions and Ar had to be added for use in the present comparison, the failure of the mechanism to generalize in any reasonable way nevertheless raises a question as to its utility and highlights the need for extreme care in applying reduced mechanisms at conditions outside of their validated ranges. Across all simulation comparisons presented here, differences in the experimental and simulated conditions somewhat limit the strength of conclusions that can be drawn; to this end, future work should be directed into determining more robust means of comparison, potentially through individualized simulation–experiment pairings or through the projection of experimental data to a set of unified P_u and ϕ conditions at which simulations can be performed.

It is additionally noted that the present S_L measurements are found to increase monotonically with T_u, continually increasing over the studied range without exhibiting the region of apparent negative temperature dependence observed in early shock-tube flame studies [31, 32]. This key difference was anticipated based on the intervening findings that the "flame structure" visible in emission images at temperatures coinciding with the region of negative temperature dependence [32, 33] was an artifact of axial distortion of those flames [34, 37]. As flame distortion leads to an increase in the flame-front area and, correspondingly, the total burning rate of the flame [41, 42], the presence of distortion in prior studies might reasonably be assumed to have had a causal relationship with the apparent negative temperature dependence observed in those works. In the present investigation, experimental refinements (*i.e.*, use of Ar–O_2 oxidizer and ignition-location tailoring) and use of the AA-LC extrapolation model would be expected to mitigate and correct those distortion effects, thus providing the monotonic results expected based on 1-D S_L calculations and reflected in the present data.

While the discontinuation of helium (He) dilution makes the present measurements more relevant to flames ignited in air, it also make the present results less-directly comparable to the ear-

lier studies [31–33]. The high thermal conductivity of He leads to relatively higher minimum ignition energies and much thicker preheat zones, both of which may affect flame dynamics. As such, that the present results do not exhibit negative temperature dependence does not strictly preclude that either phenomena identified through simulations as candidate explanations for the behavior — double flames [10, 11, 44, 72] or pyrolysis-induced over-driven flames [43] — could have been present at the conditions of those earlier studies. Revisiting experiments at precisely the conditions of the previous studies with the enhanced capabilities of the refined facility, methods, and diagnostics remains a valuable target for future experimentation.

CONCLUSIONS AND FUTURE WORK

Laminar flame speed measurements were performed for the primary reference fuels at extreme temperatures, up to and exceeding 1,000 K, for the first time. Measurements were performed using expanding flames behind reflected shocks in an imaging shock tube. Flames were ignited using LIPI and observed through custom side-wall windows using a high-speed schlieren imaging system. Area-averaged flame speeds and curvatures were extracted and used to determine the extrapolated and density-corrected value S_L through the AA-LC model.

Three empirical forms were assessed for their ability to describe the temperature dependence of S_L measurements at high T_u. The power-law form, used almost exclusively in the literature, and the exponential form were both found to result in systematic errors on the order of 10% over the range of T_u fit, and larger errors (up to 40%) when extrapolated to higher T_u. Conversely, the proposed non-Arrhenius model systematically captured the T_u over the entire fitting range and performed best of the three models better when extrapolated to higher T_u.

Comparisons between S_L measurements and predictions obtained from kinetic mechanisms identified discrepancies over all T_u conditions for the present P_u, ϕ, and oxidizer conditions. The detailed LLNL and reduced CRECK mechanisms were found to over predict the measured data by a modest amount, but greater than what could be attributed to variations in ϕ and P_u. The skeletal Nissan mechanism, on the other hand, was found to drastically under predict the measurements by a factor of 3–4.

Taken together, this work demonstrates the critical new ability to perform reliable S_L measurements over a significantly expanded range T_u. Through this and future works, the availability of S_L data at high T_u will provide new experimental targets against which kinetic mechanisms can be refined and validated. Future efforts should bring model validation and refinement efforts together with this new capability to enhance the fidelity of chemical kinetic mechanisms at the temperatures of greatest relevance to energy-system applications. Additionally, the high-T_u measurements illustrate the significant risk for error introduced when empirical models and skeletal mechanisms are applied outside the ranges over which they are validated, motivating either the use of an alternative empirical form to model the S_L–T_u relationship or the need to use an appropriately validated reaction mechanism.

ACKNOWLEDGMENT

This work was supported by the U.S. National Science Foundation under award numbers 1940865 and 2136218, contract monitor Dr. John Daily. Acquisition of the instrumentation used in this work was supported by the U.S. Army Research Office through grant numbers W911NF-20-1-0068 and W911NF-20-1-0236, contract monitor Dr. Ralph Anthenien.

PUBLICATION HISTORY

The contents of this paper are based on material included in A. J. Susa's Ph.D. dissertation [73].

REFERENCES

[1] Ferris, A. M., Susa, A. J., Davidson, D. F., and Hanson, R. K., 2019. "High-temperature laminar flame speed measurements in a shock tube". *Combustion and Flame,* ***205***, pp. 241–252.

[2] Kaiser, E. W., Yang, J., Culp, T., Xu, N., and Maricq, M. M., 2002. "Homogeneous charge compression ignition engine-out emission-does flame propagation occur in homogeneous charge compression ignition?". *International Journal of Engine Research,* ***3***(4), Aug., pp. 185–195.

[3] Juneja, H., LaPointe, L. A., Ntone, F., Lyford-Pike, E. J., and Qin, X., 2010. "Development and application of advanced combustion modeling tools for heavy duty gaseous fueled industrial spark ignition engines". In ASME 2010 Internal Combustion Engine Division Fall Technical Conference, Vol. 49446, ASMEDC, pp. 741–751.

[4] Xu, H., and LaPointe, L. A., 2013. "Calculation of laminar flame speed and autoignition delay at high temperature and pressures". In Volume 1: Large Bore Engines; Advanced Combustion; Emissions Control Systems; Instrumentation, Controls, and Hybrids, American Society of Mechanical Engineers.

[5] Sankaran, R., 2015. "Propagation velocity of a deflagration front in a preheated autoigniting mixture". In 9th US Natlonal Combustion Meeting.

[6] Pan, J., Wei, H., Shu, G., Chen, Z., and Zhao, P., 2016. "The role of low temperature chemistry in combustion mode development under elevated pressures". *Combustion and Flame,* ***174***, Dec., pp. 179–193.

[7] Krisman, A., Hawkes, E. R., and Chen, J. H., 2018. "The structure and propagation of laminar flames under autoigni-

tive conditions". *Combustion and Flame,* ***188***, Feb., pp. 399–411.

[8] Ansari, A., Jayachandran, J., and Egolfopoulos, F. N., 2019. "Parameters influencing the burning rate of laminar flames propagating into a reacting mixture". *Proceedings of the Combustion Institute,* ***37***(2), pp. 1513–1520.

[9] Faghih, M., Li, H., Gou, X., and Chen, Z., 2019. "On laminar premixed flame propagating into autoigniting mixtures under engine-relevant conditions". *Proceedings of the Combustion Institute,* ***37***(4), pp. 4673–4680.

[10] Zhang, T., Susa, A. J., Hanson, R. K., and Ju, Y., 2020. "Studies of the dynamics of autoignition assisted outwardly propagating spherical cool and double flames under shock-tube conditions". *Proceedings of the Combustion Institute,* ***38***(2), pp. 2275–2283.

[11] Zhang, T., Susa, A. J., Hanson, R. K., and Ju, Y., 2021. "Two-dimensional simulation of cool and double flame formation induced by the laser ignition under shock-tube conditions". In 12th US National Combustion Meeting, p. 1G06.

[12] Puduppakkam, K. V., Modak, A. U., Wang, C., Hodgson, D., Naik, C. V., and Meeks, E., 2020. "Generating laminar flame speed libraries for autoignition conditions". In Turbo Expo: Power for Land, Sea, and Air, Vol. 84133, ASME, p. V04BT04A004.

[13] ASTM D 2699: 2017-11, 2017. Test method for research octane number of spark-ignition engine fuel. Tech. rep., ASTM.

[14] ASTM D 2700: 2017-11, 2017. Test method for motor octane number of spark-ignition engine fuel. Tech. rep., ASTM.

[15] Szybist, J. P., and Splitter, D. A., 2020. "Impact of engine pressure-temperature trajectory on autoignition for varying fuel properties". *Applications in Energy and Combustion Science,* ***1-4***, Dec., p. 100003.

[16] University of California at San Diego, 2016. Chemical-kinetic mechanisms for combustion applications.

[17] Goodwin, D. G., Speth, R. L., Moffat, H. K., and Weber, B. W., 2021. Cantera: An object-oriented software toolkit for chemical kinetics, thermodynamics, and transport processes. Version 2.5.1.

[18] Tse, S. D., Zhu, D., and Law, C. K., 2004. "Optically accessible high-pressure combustion apparatus". *Review of Scientific Instruments,* ***75***(1), Jan., pp. 233–239.

[19] Egolfopoulos, F., Hansen, N., Ju, Y., Kohse-Höinghaus, K., Law, C., and Qi, F., 2014. "Advances and challenges in laminar flame experiments and implications for combustion chemistry". *Progress in Energy and Combustion Science,* ***43***, Aug., pp. 36–67.

[20] Metghalchi, M., and Keck, J. C., 1982. "Burning velocities of mixtures of air with methanol, isooctane, and indolene at high pressure and temperature". *Combustion and Flame,* ***48***, Jan., pp. 191–210.

[21] Ömer L. Gülder, 1984. "Correlations of laminar combustion data for alternative s.i. engine fuels". In SAE Technical Paper Series, SAE International.

[22] Xiouris, C., Ye, T., Jayachandran, J., and Egolfopoulos, F. N., 2016. "Laminar flame speeds under engine-relevant conditions: Uncertainty quantification and minimization in spherically expanding flame experiments". *Combustion and Flame,* ***163***, Jan., pp. 270–283.

[23] Halter, F., Chen, Z., Dayma, G., Bariki, C., Wang, Y., Dagaut, P., and Chauveau, C., 2020. "Development of an optically accessible apparatus to characterize the evolution of spherically expanding flames under constant volume conditions". *Combustion and Flame,* ***212***, Feb., pp. 165–176.

[24] Wang, Y., Movaghar, A., Wang, Z., Liu, Z., Sun, W., Egolfopoulos, F. N., and Chen, Z., 2020. "Laminar flame speeds of methane/air mixtures at engine conditions: Performance of different kinetic models and power-law correlations". *Combustion and Flame,* ***218***, Aug., pp. 101–108.

[25] Lawson, R., Gururajan, V., Movaghar, A., and Egolfopoulos, F. N., 2020. "Autoignition of reacting mixtures at engine-relevant conditions using confined spherically expanding flames". *Proceedings of the Combustion Institute,* ***38***(2), pp. 2285–2293.

[26] Akram, M., and Kumar, S., 2012. "Measurement of laminar burning velocity of liquified petrolium gas air mixtures at elevated temperatures". *Energy & Fuels,* ***26***(6), June, pp. 3267–3274.

[27] Konnov, A. A., Mohammad, A., Kishore, V. R., Kim, N. I., Prathap, C., and Kumar, S., 2018. "A comprehensive review of measurements and data analysis of laminar burning velocities for various fuel+air mixtures". *Progress in Energy and Combustion Science,* ***68***, Sept., pp. 197–267.

[28] Susa, A. J., and Hanson, R. K., Accepted. "Simultaneous side-wall schlieren and emission imaging of autoignition phenomena in conventional and constrained-reaction-volume shock-tube experiments". *Proceedings of the Combustion Institute*.

[29] Singhan Ramamoorthy, V., 2014. "High-speed imaging of autoignition in a high-pressure shock tube". Master's thesis, Universität Duisburg Essen.

[30] Shao, J., Choudhary, R., Susa, A. J., Davidson, D. F., and Hanson, R. K., 2021. "High-speed imaging of n-heptane ignition in a high-pressure shock tube". *Proceedings of the Combustion Institute,* ***38***(1), pp. 911–918.

[31] Susa, A. J., Ferris, A. M., Davidson, D. F., and Hanson, R. K., 2019. "Experimental shock tube measurements of laminar burning velocity of n-heptane and iso-octane in the negative temperature coefficient regime". In AIAA Scitech 2019 Forum, American Institute of Aeronautics and Astronautics, p. 0460.

[32] Susa, A. J., Ferris, A. M., Davidson, D. F., and Hanson,

R. K., 2019. "Experimental observation of negative temperature dependence in iso-octane burning velocities". *AIAA Journal,* ***57***(10), pp. 4476–4481.

[33] Susa, A. J., Ferris, A. M., Davidson, D. F., and Hanson, R. K., 2019. "Experimental measurement of laminar burning velocity of n-heptane at variable extents of reactions in a shock tube". In 32nd International Symposium on Shock Waves, pp. 917–925.

[34] Susa, A. J., and Hanson, R. K., 2022. "Distortion of expanding n-heptane flames at high unburned-gas temperatures behind reflected shocks". *Combustion and Flame,* ***237***, Mar., p. 111842.

[35] Susa, A. J., 2022. *Meta-Analysis of Conditions Producing Stable Flames in a Shock Tube*. Stanford University, ch. 5, pp. 93–103.

[36] Susa, A. J., and Hanson, R. K., 2022. "Flame image velocimetry: Seedless characterization of post-reflected-shock velocities in a shock tube". *Experiments in Fluids*.

[37] Susa, A. J., Zheng, L., Nygaard, Z. D., and Hanson, R. K., 2022. "End-wall effects on freely propagating flames in a shock tube". In AIAA Scitech Forum, American Institute of Aeronautics and Astronautics, p. 2346.

[38] Susa, A. J., 2022. *Side-wall imaging flame test section (SWIFT)*. Stanford University, ch. 6, pp. 105–129.

[39] Zheng, L., Susa, A. J., and Hanson, R. K., 2022. "Methodology of designing compact schlieren systems using off-axis parabolic mirrors". *Applied Optics,* ***61***, pp. 4857–4864.

[40] Susa, A. J., Zheng, L., and Hanson, R. K., 2021. "Schlieren-based measurements of propane flame speeds at extreme temperatures". In 12th US National Combustion Meeting, p. 1G05.

[41] Susa, A. J., Zheng, L., and Hanson, R. K., Accepted. "Measurements of propane-O_2-Ar laminar flame speeds at temperatures exceeding1,000 K in a shock tube". *Proceedings of the Combustion Institute*.

[42] Susa, A. J., 2022. *Measurements of Propane Flame Speeds at Extreme Temperatures*. Stanford University, ch. 8, pp. 147–166.

[43] Yang, Q., Chen, Z., Susa, A. J., Hanson, R. K., and Zhao, P., 2021. "Thermal-pyrolysis induced over-driven flame and its potential role in the negative-temperature dependence of iso-octane flame speed at elevated temperatures". *Combustion and Flame,* ***223***, Jan., pp. 65–76.

[44] Zhang, T., Susa, A. J., Hanson, R. K., and Ju, Y., Accepted. "Two-dimensional simulation of cool and double flame formation induced by the laser ignition under shock-tube conditions". *Proceedings of the Combustion Institute*.

[45] Susa, A. J., 2022. "High-speed imaging studies of flames in a shock tube: Refined techniques and new applications". PhD thesis, Stanford University.

[46] Wang, S., Parise, T., Johnson, S. E., Davidson, D. F., and Hanson, R. K., 2017. "A new diagnostic for hydrocarbon fuels using 3.41-um diode laser absorption". *Combustion and Flame,* ***186***, Dec., pp. 129 – 139.

[47] Campbell, M. F., Owen, K. G., Davidson, D. F., and Hanson, R. K., 2017. "Dependence of calculated postshock thermodynamic variables on vibrational equilibrium and input uncertainty". *Journal of Thermophysics and Heat Transfer,* ***31***(3), pp. 586–608.

[48] Hong, Z., Pang, G. A., Vasu, S. S., Davidson, D. F., and Hanson, R. K., 2009. "The use of driver inserts to reduce non-ideal pressure variations behind reflected shock waves". *Shock Waves,* ***19***(2), pp. 113–123.

[49] Grogan, K., and Ihme, M., 2020. "Stanshock: A gas-dynamic model for shock tube simulations with non-ideal effects and chemical kinetics". *Shock Waves,* ***30***(4), Jan., pp. 425–438.

[50] Weinberg, F. J., and Wilson, J., 1971. "A preliminary investigation of the use of focused laser beams for minimum ignition energy studies". *Proceedings of the Royal Society of London. A. Mathematical and Physical Sciences,* ***321***(1544), Jan., pp. 41–52.

[51] Phuoc, T. X., and White, F. P., 2002. "An optical and spectroscopic study of laser-induced sparks to determine available ignition energy". *Proceedings of the Combustion Institute,* ***29***(2), Jan., pp. 1621–1628.

[52] Phuoc, T. X., 2006. "Laser-induced spark ignition fundamental and applications". *Optics and Lasers in Engineering,* ***44***(5), May, pp. 351–397.

[53] Settles, G. S., 2001. *Specialized schlieren techniques*. Springer Berlin Heidelberg, ch. 5, pp. 116–118.

[54] Ottomatic GmbH, 2019. pycine. https://github.com/ottomatic-io/pycine.

[55] van der Walt, S., Schönberger, J. L., Nunez-Iglesias, J., Boulogne, F., Warner, J. D., Yager, N., Gouillart, E., Yu, T., and the scikit-image contributors, 2014. "scikit-image: image processing in Python". *PeerJ,* ***2***, 6, p. e453.

[56] Zhao, X., Luo, Q., Han, B., and Li, X., 2009. "An image distortion correction algorithm based on quadrilateral fractal approach controlling points". In 2009 4th IEEE Conference on Industrial Electronics and Applications, IEEE.

[57] Zheng, L., Lawlor, B., Katko, B., McGuire, C., Zanteson, J., and Eliasson, V., 2020. "Image processing and edge detection techniques to quantify shock wave dynamics experiments". *Experimental Techniques,* ***45***(4), dec, pp. 483–495.

[58] Kass, M., Witkin, A., and Terzopoulos, D., 1988. "Snakes: Active contour models". *International Journal of Computer Vision,* ***1***(4), Jan., pp. 321–331.

[59] Chen, Z., 2011. "On the extraction of laminar flame speed and markstein length from outwardly propagating spherical flames". *Combustion and Flame,* ***158***(2), Feb., pp. 291–300.

[60] Chen, Z., 2015. "On the accuracy of laminar flame speeds measured from outwardly propagating spherical flames: Methane/air at normal temperature and pressure". *Combustion and Flame,* ***162***(6), June, pp. 2442–2453.
[61] Savitzky, A., and Golay, M. J., 1964. "Smoothing and differentiation of data by simplified least squares procedures.". *Analytical chemistry,* ***36***(8), pp. 1627–1639.
[62] Virtanen, P., and et al., 2020. "SciPy 1.0: Fundamental Algorithms for Scientific Computing in Python". *Nature Methods,* ***17***, pp. 261–272.
[63] Burke, M. P., Chen, Z., Ju, Y., and Dryer, F. L., 2009. "Effect of cylindrical confinement on the determination of laminar flame speeds using outwardly propagating flames". *Combustion and Flame,* ***156***(4), Apr., pp. 771–779.
[64] Stevens, F. W., 1923. A constant pressure bomb. Tech. Rep. 176, National Advisory Committee for Aeronautics.
[65] Mehl, M., Pitz, W. J., Sjöberg, M., and Dec, J. E., 2009. "Detailed kinetic modeling of low-temperature heat release for PRF fuels in an HCCI engine". In SAE Technical Paper Series, SAE International.
[66] Mehl, M., Pitz, W. J., Westbrook, C. K., and Curran, H. J., 2011. "Kinetic modeling of gasoline surrogate components and mixtures under engine conditions". *Proceedings of the Combustion Institute,* ***33***(1), pp. 193–200.
[67] Stagni, A., Cuoci, A., Frassoldati, A., Faravelli, T., and Ranzi, E., 2013. "Lumping and reduction of detailed kinetic schemes: an effective coupling". *Industrial & Engineering Chemistry Research,* ***53***(22), dec, pp. 9004–9016.
[68] Ranzi, E., Frassoldati, A., Stagni, A., Pelucchi, M., Cuoci, A., and Faravelli, T., 2014. "Reduced kinetic schemes of complex reaction systems: Fossil and biomass-derived transportation fuels". *International Journal of Chemical Kinetics,* ***46***(9), jul, pp. 512–542.
[69] Stagni, A., Frassoldati, A., Cuoci, A., Faravelli, T., and Ranzi, E., 2016. "Skeletal mechanism reduction through species-targeted sensitivity analysis". *Combustion and Flame,* ***163***, jan, pp. 382–393.
[70] Tsurushima, T., and Nissan Motor Co., Ltd., 2009. "A new skeletal PRF kinetic model for HCCI combustion". *Proceedings of the Combustion Institute,* ***32***(2), pp. 2835–2841.
[71] Dong, S., Wagnon, S. W., Maffei, L. P., Kukkadapu, G., Nobili, A., Mao, Q., Pelucchi, M., Cai, L., Zhang, K., Raju, M., Chatterjee, T., Pitz, W. J., Faravelli, T., Pitsch, H., Senecal, P. K., and Curran, H. J., 2022. "A new detailed kinetic model for surrogate fuels: C3mechv3.3". *Applications in Energy and Combustion Science,* ***9***, Mar., p. 100043.
[72] Ju, Y., 2021. "Understanding cool flames and warm flames". *Proceedings of the Combustion Institute,* ***38***(1), pp. 83–119.
[73] Susa, A. J., 2022. *Primary-Reference-Fuel Flame Speeds at Extreme Temperatures*. Stanford University, ch. 9, pp. 167–178.

APPENDIX A: AA-LC FITS AND TABULATED DATA

This appendix contains data obtained at intervening steps during data processing along with tabulated details of the experimental conditions and results in addition to the result plots presented earlier in the manuscript. Figures 9 and 10 show the raw $\bar{S}_b$-vs.-$\bar{\kappa}$ data for all experiments reported in the present work, along with the linear fits representing the AA-LC extrapolation model. The plots shown in Fig. 7 are a subset of those presented here.

Figures 11 and 12 display the values of S_b^0 and L_b corresponding to the AA-LC fits, along with the value S_u^0 (*i.e.,* S_L) converted through Eqn. 10. Data points are colored to match the corresponding fits in Fig. 9 and 10. Values of the Markstein length (L_b), obtained from the slope of the $\bar{S}_b$–$\bar{\kappa}$ fits, show a relatively large degree of scatter but very small absolute magnitude. As a result of the small magnitude and limited extent of $\bar{\kappa}$ over which the extrapolation to zero curvature must be performed, the scatter in the L_b values does not manifest as corresponding scatter in the values S_b^0. Even so, the uncertainty of the slope for each fit is the primary source contributing to the S_b^0 confidence interval, represented as shaded regions in Fig. 9 and 10 and vertical error bars in Fig. 8.

Finally, Tables 2 and 3 contain the complete details of the experimental conditions and measurement results for all experiments reported in this work, along with associated uncertainties. The uncertainty in T_u accounts both for the uncertainty in the shock speed input to FROSH [47] as well as that of the mixture composition, defined as the deviation of the measured ϕ from the nominal value of unity. P_u uncertainty includes contributions both from the shock speed and the difference between the FROSH-calculated and Kistler-measured values of P_5. The uncertainty in ϕ is dominated by the contribution from P_5 but also includes the fluctuation of the fuel mole fraction measured during each experiment; *in situ* measured ϕ values are unavailable at the lowest T_u conditions due to the absorption cross sections having not yet been characterized at such low temperatures [46].

Tabulated values of S_b^0 and L_b were obtained using the fits of Fig. 9 and 10 and reflect those values plotted in Fig. 11 and 12. Uncertainties listed in the table include only that of the AA-LC fit (reported at the 95% confidence level). The equilibrium unburned- to burned-gas density ratios used in this work to convert from the burned- to unburned-gas frame of reference are also included, as well as the final values of S_L reported in Fig. 8.

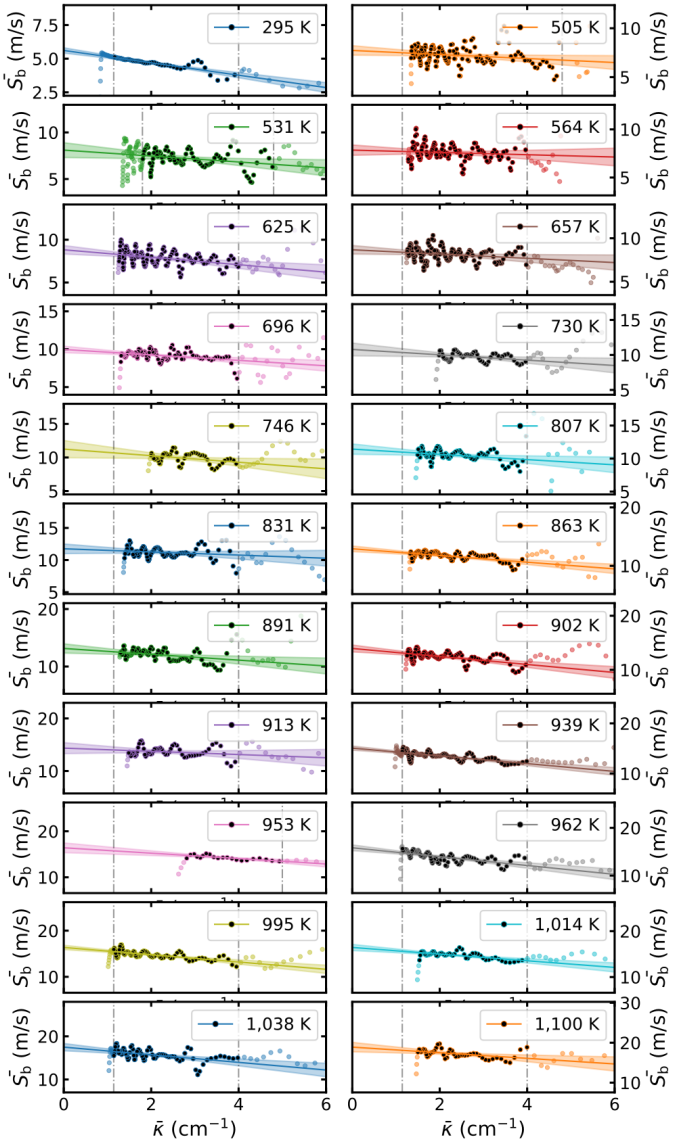

FIGURE 9: *N*-HEPTANE DATA AND AA-LC FITS

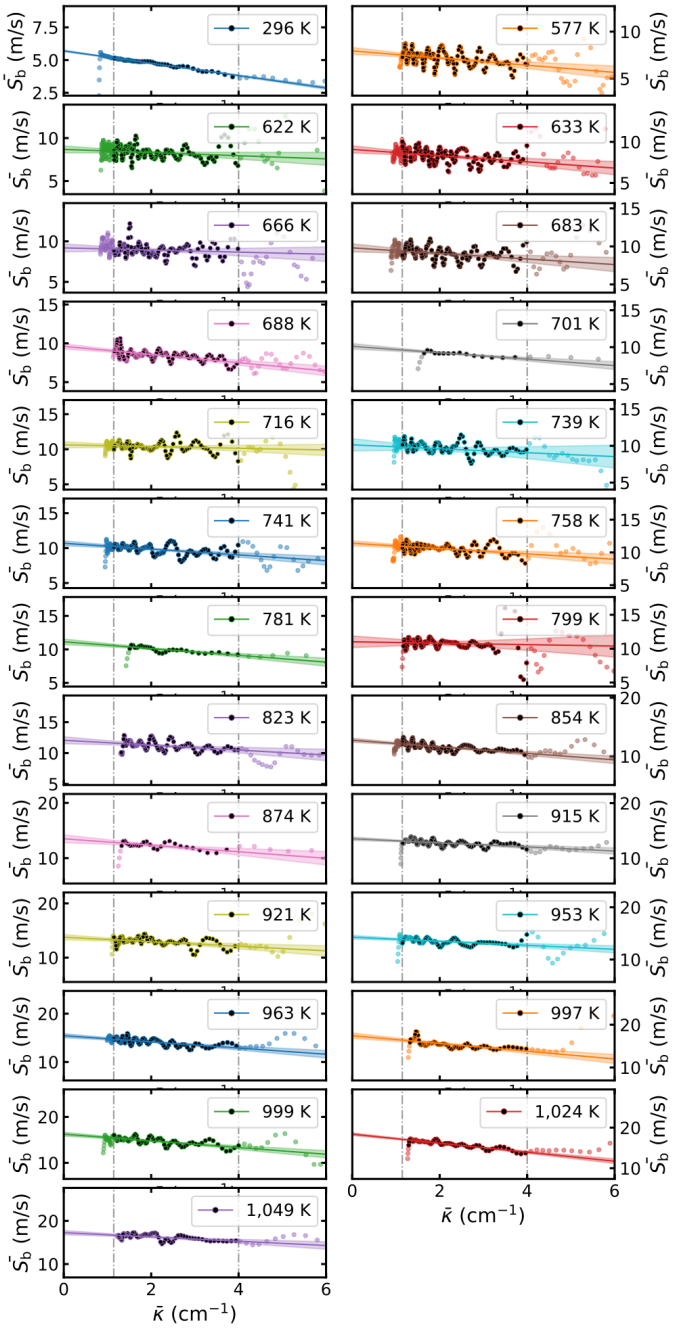

FIGURE 10: *ISO*-OCTANE DATA AND AA-LC FITS

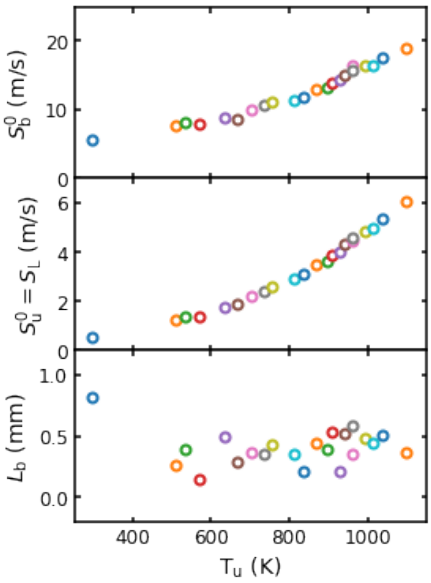

FIGURE 11: *N*-HEPTANE FLAME SPEEDS AND MARKSTEIN LENGTHS

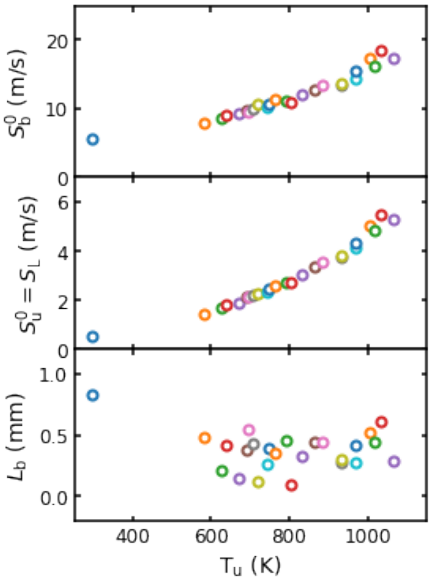

FIGURE 12: *ISO*-OCTANE FLAME SPEEDS AND MARKSTEIN LENGTHS

TABLE 2: *N*-HEPTANE EXPERIMENTAL CONDITIONS AND RESULTS

T_u			P_u			ϕ			S_b^0			L_b			ρ_u/ρ_b	S_L		
(K	±	%)	(atm	±	%)	(-	±	%)	(m/s	±	%)	(mm	±	mm)	(-)	(m/s	±	%)
295	±	-	0.93	±	-	-	±	-	5.61	±	3.0	0.82	±	0.14	10.3	0.55	±	3.0
505	±	1.0	1.02	±	3.7	-	±	-	7.43	±	6.6	0.08	±	0.25	6.27	1.19	±	6.6
531	±	1.1	1.02	±	4.1	-	±	-	7.92	±	5.9	0.33	±	0.23	5.99	1.32	±	5.9
564	±	1.4	1.06	±	5.2	-	±	-	7.70	±	7.4	0.07	±	0.29	5.68	1.36	±	7.4
625	±	1.2	1.02	±	4.7	-	±	-	8.82	±	4.8	0.49	±	0.21	5.19	1.70	±	4.8
657	±	1.3	1.03	±	5.2	0.86	±	5.5	8.67	±	4.8	0.28	±	0.21	4.97	1.74	±	4.8
696	±	1.5	0.99	±	5.8	0.92	±	6.0	9.97	±	3.6	0.36	±	0.16	4.72	2.11	±	3.6
730	±	1.1	1.01	±	4.6	0.97	±	4.7	10.8	±	7.1	0.35	±	0.25	4.54	2.38	±	7.1
746	±	1.0	0.98	±	4.1	0.94	±	4.3	11.2	±	9.5	0.43	±	0.34	4.46	2.52	±	9.5
807	±	2.4	0.98	±	4.0	0.85	±	4.4	11.4	±	5.8	0.35	±	0.24	3.93	2.91	±	5.8
831	±	2.5	0.97	±	4.1	0.85	±	4.3	11.8	±	5.4	0.21	±	0.23	3.82	3.08	±	5.4
863	±	2.6	0.99	±	4.5	0.86	±	4.7	12.9	±	3.1	0.44	±	0.14	3.73	3.46	±	3.1
891	±	2.7	0.99	±	4.8	0.86	±	4.9	13.1	±	5.2	0.39	±	0.23	3.63	3.62	±	5.2
902	±	2.3	0.96	±	3.4	0.86	±	3.6	14.0	±	3.8	0.53	±	0.17	3.59	3.88	±	3.8
913	±	1.2	1.03	±	5.2	0.90	±	5.2	14.4	±	6.1	0.21	±	0.25	3.77	3.81	±	6.1
939	±	3.3	0.99	±	6.1	0.87	±	6.3	15.1	±	2.3	0.51	±	0.11	3.50	4.30	±	2.3
953	±	0.8	1.00	±	4.1	1.05	±	4.1	16.4	±	5.3	0.36	±	0.14	3.69	4.44	±	5.3
962	±	3.3	0.98	±	6.0	0.87	±	6.2	15.8	±	3.2	0.59	±	0.15	3.43	4.61	±	3.2
995	±	3.0	1.00	±	5.7	0.89	±	5.8	16.4	±	2.4	0.48	±	0.11	3.37	4.86	±	2.4
1,014	±	3.0	0.98	±	5.2	0.88	±	5.5	16.5	±	3.4	0.44	±	0.14	3.31	4.97	±	3.4
1,038	±	3.0	0.99	±	6.0	0.90	±	6.1	17.5	±	4.1	0.51	±	0.19	3.28	5.34	±	4.1
1,100	±	3.2	0.96	±	6.4	0.90	±	6.5	18.9	±	5.3	0.37	±	0.21	3.13	6.04	±	5.3

TABLE 3: *ISO*-OCTANE EXPERIMENTAL CONDITIONS AND RESULTS

T_u			P_u			ϕ			S_b^0			L_b			ρ_u/ρ_b	S_L		
(K	±	%)	(atm	±	%)	(-	±	%)	(m/s	±	%)	(mm	±	mm)	(-)	(m/s	±	%)
296	±	-	1.00	±	-	-	±	-	5.70	±	0.8	0.83	±	0.04	10.3	0.56	±	0.8
577	±	1.6	0.98	±	5.8	-	±	-	7.95	±	3.9	0.48	±	0.18	5.57	1.43	±	3.9
622	±	1.5	1.04	±	4.8	0.97	±	5.1	8.69	±	3.9	0.21	±	0.18	5.17	1.68	±	3.9
633	±	0.9	1.03	±	2.5	0.95	±	3.2	9.08	±	4.0	0.42	±	0.18	5.05	1.80	±	4.0
666	±	1.0	1.06	±	4.2	0.98	±	4.6	9.19	±	4.5	0.14	±	0.20	4.93	1.87	±	4.5
683	±	0.5	0.94	±	1.2	0.94	±	2.4	9.81	±	4.5	0.37	±	0.20	4.81	2.04	±	4.5
688	±	1.8	0.97	±	6.7	0.91	±	7.0	9.61	±	3.0	0.55	±	0.14	4.78	2.01	±	3.0
701	±	1.2	1.00	±	4.7	0.96	±	5.0	10.1	±	3.0	0.43	±	0.12	4.71	2.15	±	3.0
716	±	0.4	0.98	±	3.7	1.08	±	3.9	10.6	±	3.4	0.12	±	0.16	4.73	2.25	±	3.4
739	±	1.5	1.03	±	3.9	0.94	±	4.3	10.1	±	6.9	0.26	±	0.32	4.40	2.31	±	6.9
741	±	1.5	0.95	±	3.9	0.93	±	4.2	10.7	±	2.7	0.39	±	0.12	4.38	2.44	±	2.7
758	±	0.8	1.06	±	4.0	1.02	±	4.2	11.4	±	2.9	0.36	±	0.14	4.44	2.57	±	2.9
781	±	1.3	0.94	±	5.2	0.90	±	5.2	11.1	±	3.0	0.45	±	0.12	4.29	2.59	±	3.0
799	±	1.6	0.98	±	4.3	0.94	±	4.6	11.0	±	6.6	0.10	±	0.30	4.12	2.67	±	6.6
823	±	1.2	1.03	±	4.9	0.93	±	4.9	12.1	±	3.9	0.33	±	0.17	4.11	2.94	±	3.9
854	±	1.8	1.01	±	6.9	0.91	±	6.9	12.7	±	2.2	0.44	±	0.10	3.99	3.19	±	2.2
874	±	1.3	0.98	±	5.2	0.95	±	5.3	13.5	±	4.4	0.44	±	0.19	3.91	3.45	±	4.4
915	±	1.3	1.03	±	5.6	0.91	±	5.7	13.5	±	1.9	0.27	±	0.09	3.77	3.59	±	1.9
921	±	1.5	0.98	±	6.0	0.92	±	6.0	13.8	±	3.0	0.30	±	0.14	3.75	3.67	±	3.0
953	±	1.4	1.00	±	5.7	0.91	±	5.7	14.3	±	2.1	0.27	±	0.10	3.64	3.91	±	2.1
963	±	1.6	0.96	±	4.6	0.96	±	4.8	15.4	±	2.3	0.41	±	0.10	3.56	4.33	±	2.3
997	±	1.6	1.03	±	4.7	0.97	±	4.7	17.4	±	3.1	0.52	±	0.13	3.47	5.02	±	3.1
999	±	1.3	0.99	±	5.5	0.90	±	5.5	16.2	±	2.2	0.45	±	0.10	3.51	4.63	±	2.2
1,024	±	1.7	0.97	±	4.6	0.95	±	4.7	18.4	±	1.5	0.60	±	0.06	3.38	5.44	±	1.5
1,049	±	1.6	0.99	±	6.8	0.93	±	6.8	17.3	±	2.4	0.29	±	0.11	3.38	5.11	±	2.4